

MIT Open Access Articles

Screened Expanding Turning Vane Concept

The MIT Faculty has made this article openly available. **Please share** how this access benefits you. Your story matters.

Citation: Drela, Mark et al. "Screening Expanding Turning Vane Concept." AIAA Scitech 2019 Forum. January 2019, San Diego, California, AIAA Scitech 2019 Forum, January 2019 © 2019 The Author(s)

As Published: <http://dx.doi.org/10.2514/6.2019-1613>

Publisher: American Institute of Aeronautics and Astronautics

Persistent URL: <https://hdl.handle.net/1721.1/123882>

Version: Author's final manuscript: final author's manuscript post peer review, without publisher's formatting or copy editing

Terms of use: Creative Commons Attribution-Noncommercial-Share Alike



Screened expanding turning-vane concept *

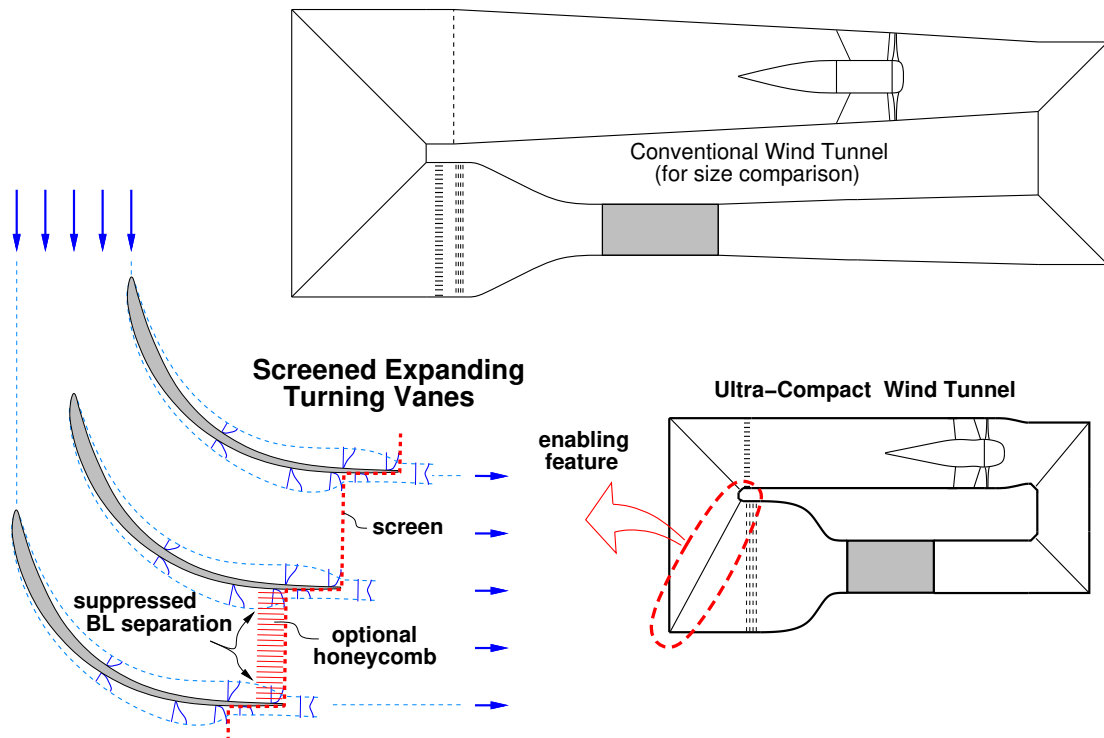
Mark Drela[†], Arthur Huang[‡], David Darmofal[§]

*Department of Aeronautics and Astronautics
Massachusetts Institute of Technology, Cambridge, MA, 02139, USA*

Abstract

The paper presents the screened expanding corner vane concept, which can turn a channel flow by 90° , while simultaneously increasing the flow area by at least a factor of two and thus halving the mean velocity, all without incurring any significant flow separation. The concept is demonstrated experimentally, and investigated with analytical and computational models. One target application is an ultra-compact closed-circuit wind tunnel, whose overall length is roughly half that of a conventional wind tunnel with the same test section.

Graphic abstract



*Published in *Experiments in Fluids*, 2020, doi: 10.1007/s00348-020-2910-3

[†]Terry J. Kohler Professor

[‡]PhD student

[§]Professor

List of symbols

A	Channel flow area	y, z	Channel transverse coordinates
c	Vane chord	β	Screen open-area fraction
C_p	Pressure coefficient = $(p-p_0)/\frac{1}{2}\rho V_0^2$	Δ^*	BL displacement area = $\int(1-\frac{V}{V_e})dA$
C_{pT}	Total pressure coefficient = $(p_T-p_{T0})/\frac{1}{2}\rho V_0^2$	Θ	BL momentum area = $\int(1-\frac{V}{V_e})\frac{V}{V_e}dA$
f	BL velocity fraction	η	Screen diffraction ratio = V_{t2}/V_{t1}
g	BL area fraction	ρ	Density
H	BL shape parameter = Δ^*/Θ	$(\)_0$	Inviscid flow upstream of cascade
K	Screen pressure drop coefficient	$(\)_1$	Flow immediately upstream of screen
$\hat{\mathbf{n}}$	Unit vector normal to screen	$(\)_2$	Flow immediately downstream of screen
p	Static pressure	$(\)_3$	Mixed-out flow far downstream of cascade
p_T	Total pressure = $p + \frac{1}{2}\rho V^2$	$(\)_e$	Boundary layer (BL) edge quantity
\mathcal{R}_A	Outlet/inlet area expansion ratio = A_3/A_0	$(\)_n$	Component normal to screen
\mathcal{R}_{Δ^*}	Outlet/inlet blockage ratio = $(\Delta_2^*/A_2)/(\Delta_0^*/A_0)$	$(\)_t$	Component tangential to screen
V	Velocity magnitude = $ \mathbf{V} $	$(\)_\infty$	Room ambient
\mathbf{V}	Velocity vector		

1 Introduction

Conventional closed-circuit wind tunnels have almost invariably employed separate diffuser and turning-vane sections, as reviewed by Bradshaw and Pankhurst [1]. Compact tunnels have traditionally employed wide-angle diffusers in which separation is prevented by screens, typically at the cost of increased tunnel drive power [2],[3],[4].

One notable exception to these traditional practices is the relatively recent wind tunnel design by Lindgren and Johansson [5], where part of the diffusion task is carried out by “expanding” corner vanes which have a significant area increase and hence velocity decreases. The task of the diffusers is thereby reduced, so that they can be made shorter, and for a given test-section size, the overall tunnel size can be reduced. The experimental measurements of Lindgren et al [6] indicate that the area increase ratio is limited to roughly 1.4 or 1.5; else, the vane cascade losses become excessive, which limits how much tunnel size reduction can be realized in practice. From compressor design experience it was also expected that separation will typically begin at the vane/wall intersections as discussed by Lei et al [7]. This indicates that further conservatism in the vane area expansion ratio is needed.

The screened-vane concept presented here considerably increases the tolerable area expansion ratio by the use of a screen installed over the exit of each vane passage, perpendicular to the outlet flow, as diagrammed in Fig. 1. The screen suppresses any upstream separation, or at least contains the separation entirely inside the vane passage, so that the outlet does not exhibit any reversed flow. In effect, each vane passage then not only turns the flow, but also functions as a wide-angle diffuser with zero added length. It should also be mentioned that a simpler straight screen (without the zig-zag shape) over the cascade outlet would not be suitable, since the screen’s diffraction effect would then produce a total pressure gradient across the entire channel, as described by Greitzer et al. [8] and Elder [9]. To reduce outlet streamwise vorticity, a honeycomb can also be incorporated into the vanes as sketched in Fig. 1. However, this is seen as secondary to the screen’s primary function of suppressing flow separation. Hence, the effects of incorporating a honeycomb in the vanes will not be examined here.

The topic of this paper was motivated by the current (2020) project to replace the 1935-vintage Wright Brothers Wind Tunnel with an all-new tunnel (called the New WBWT) in the same site.

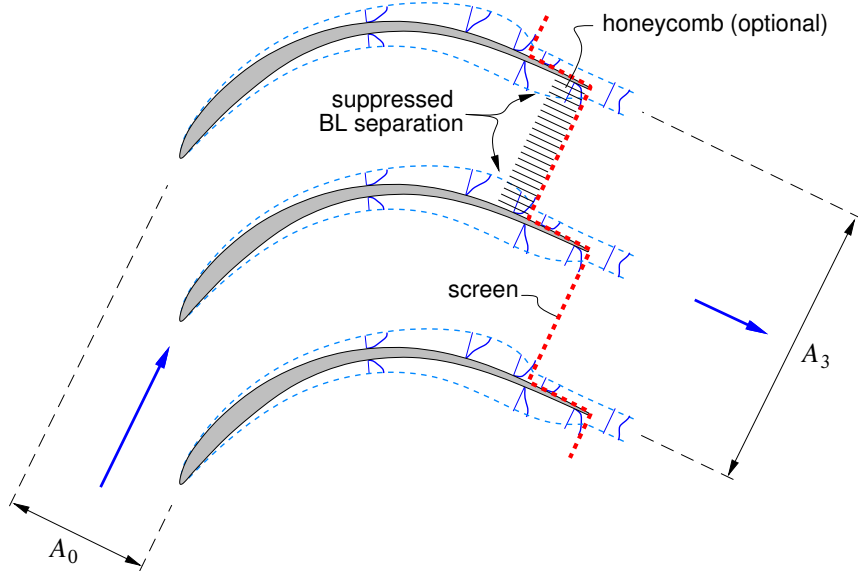


Figure 1: Screened expanding turning vane cascade.

Surrounding buildings put hard constraints on the overall length and width of the tunnel, so in the design study, all possible means to minimize the tunnel circuit size were examined. The design objective was to give the largest possible test-section size for the fixed tunnel footprint and the chosen 8:1 contraction ratio. Tunnel layout studies indicated that the most compact design (and hence the largest test section) is produced if expanding corner vanes are used in corner 4, with the large area ratio of $\mathcal{R}_A = 30/16 = 1.875$ enabled by the vane-outlet screen. Also contributing to the tunnel compactness are 2D-type diffusers with the width fixed and only the height increasing, which was also a feature in the novel tunnel design of Lindgren and Johansson [5]. The third diffuser after the fan is particularly aggressive, which is enabled by a conventional fin-tube heat exchanger at its end which also functions as a diffuser screen. Finally, the settling chamber and contraction are in effect combined into one progressively increasing contraction which starts at the last screen, and which is computationally designed for the shortest possible length without incurring flow separation.

Fig. 2 shows the extremely compact size of the New WBWT which is enabled by these design features, and in particular the screened expanding vane concept. For comparison, Fig. 2 also shows the conventional-design NASA 14×22 tunnel [10], scaled to 50% for the same test-section volume, and a notional traditional compact tunnel using a screened wide-angle diffuser. The New WBWT has an estimated power factor of 0.35, compared to an estimated 0.30 value for a conventional tunnel of the same contraction ratio and the same number of flow-conditioning screens. This $\sim 17\%$ power increase is deemed an acceptable penalty for the large test section which is realized given the small tunnel footprint. Reduced construction costs for a given tunnel capability are a clear side benefit.

The focus on this paper will be to identify the key parameters of the screened expanding turning vane, and also identify and characterize its design trade-offs. The performance of the vane will be demonstrated through experiment and 3D CFD Reynolds-Averaged Navier–Stokes computations.

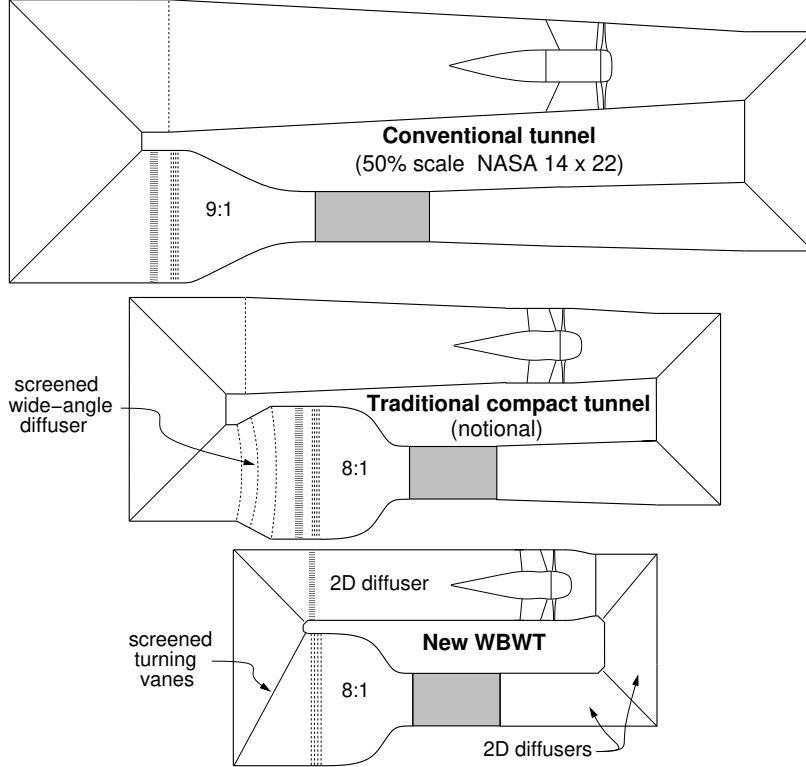


Figure 2: Size comparison of a conventional tunnel, a traditional compact tunnel, and the New WBWT ultra-compact tunnel enabled by the screened turning vanes in corner 4. Test-section volumes are the same. The New WBWT’s 2D diffusers expand only vertically

2 Flow modeling

2.1 Computational modeling

The screen’s effect on the flow is represented via its pressure drop coefficient and refraction ratio,

$$K \equiv \frac{p_2 - p_1}{\frac{1}{2}\rho_1 V_{n_1}^2} \quad (1)$$

$$\eta \equiv \frac{V_{t_2}}{V_{t_1}} \quad (2)$$

which can be obtained for any given screen from pressure and velocity–direction measurements. The 3D CFD results to be presented here were computed with Fluent ANSYS [11], in which the screen was modeled as a plane of momentum sources with specified K and η values. The local source strengths depend on the local upstream screen-normal dynamic pressure and flow direction. The screen-normal and tangential velocities are computed as:

$$V_{n_1} = \mathbf{V}_1 \cdot \hat{\mathbf{n}} \quad (3)$$

$$\mathbf{V}_{t_1} = \mathbf{V}_1 - V_{n_1} \hat{\mathbf{n}} \quad (4)$$

where \mathbf{V}_1 is the local velocity taken from the solution just upstream of the screen, and the screen-normal vector $\hat{\mathbf{n}}$ is specified. The momentum source per unit volume (in effect a body force) is

then computed by invoking the K and η definitions.

$$\mathbf{F} = -\frac{1}{2}\rho_1 V_{n_1}^2 K \hat{\mathbf{n}} - \rho_1 V_{n_1} \mathbf{V}_{t_1} (1 - \eta) \quad (5)$$

The 2D CFD results presented here were computed using the MISES viscous/inviscid code [12], which was modified by the inclusion of the above momentum source model into its Euler equation formulation. The momentum sources were also incorporated into the MISES integral boundary layer model, as originally employed for analyzing the aerodynamic impacts of boundary layer flows through heat exchangers [13].

2.2 Parallel flow model

To examine the effect of the area expansion ratio and screen pressure drop on the ability of the vane row to suppress separation, we consider the simplified quasi-1D model diagrammed in Fig. 3. The tunnel wall boundary layer (BL) is idealized as a streamtube with a velocity which is a fraction

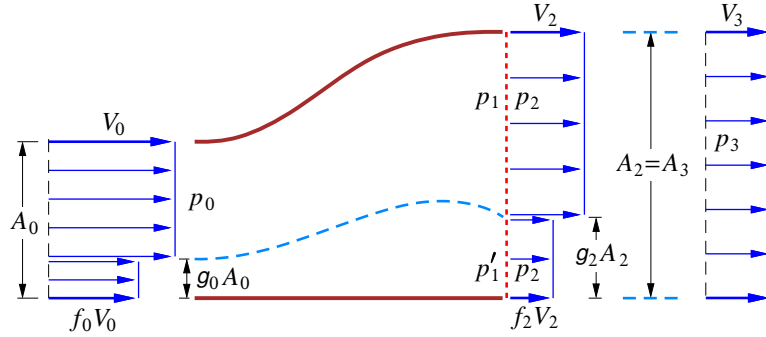


Figure 3: 2D parallel-flow model within a passage of a screened expanding vane cascade. Station 3 is at hypothetical mixed-out state

f of the core flow velocity, and with a thickness which is a fraction g of the overall channel height. One rational way to set these for a given wall BL is to match the actual known BL displacement and momentum areas Δ^* , Θ and channel area A . This gives:

$$f = \frac{\Theta}{\Delta^*} = \frac{1}{H} \quad (6)$$

$$g = \frac{\Delta^*}{A} \frac{1}{1-f} = \frac{\Delta^*}{A} \frac{H}{H-1} \quad (7)$$

so that for a typical turbulent BL with $H \simeq 1.4$ we have $f \simeq 0.7$ and $g = 3.5 \Delta^*/A$.

Low-speed inviscid calculation results for the two-streamtube model flow in Fig. 4 show that the flow disturbance is almost entirely upstream of the screen, and the upstream screen-face pressure has two distinct values in the two streamtubes, denoted here by p_1 and p'_1 . Note also that $p'_1 < p_1$, which is the mechanism which accelerates the slower moving streamtube into the screen and thus suppresses its separation. In contrast, the downstream flow is almost parallel and at one pressure p_2 .

Applying mass conservation and Bernoulli equations (with screen pressure drops) between stations 0 and 2 for each streamtube, we obtain:

$$\rho V_0 A_0 (1 - g_0) = \rho V_2 A_2 (1 - g_2) \quad (8)$$

$$\rho V_0 A_0 f_0 g_0 = \rho V_2 A_2 f_2 g_2 \quad (9)$$

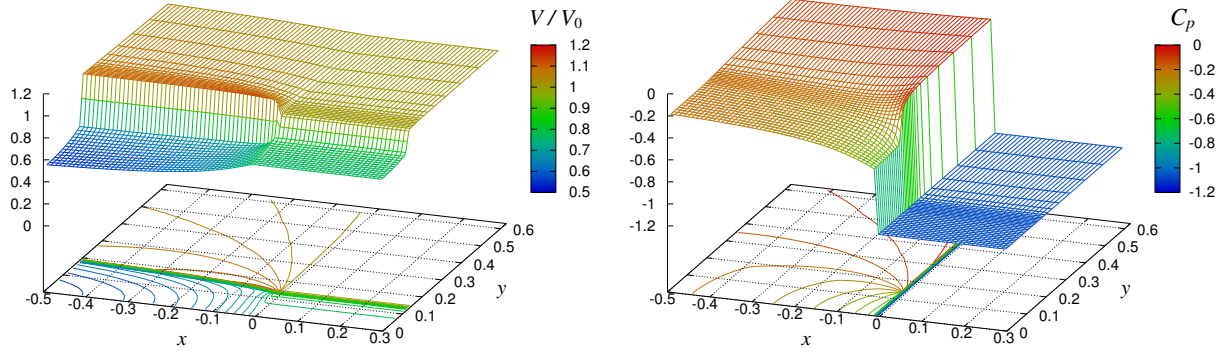


Figure 4: Velocity and static pressure fields of a two-streamtube low-speed inviscid flow with $f_0=0.5$ and $g_0 \ll 1$, interacting with a screen located at $x=0$, with parameters $K=1.0$ and $\eta=0.78$

$$p_0 + \frac{1}{2}\rho V_0^2 = p_2 + \frac{1}{2}\rho V_2^2(1+K) \quad (10)$$

$$p_0 + \frac{1}{2}\rho V_0^2 f_0^2 = p_2 + \frac{1}{2}\rho V_2^2 f_2^2(1+K), \quad (11)$$

which can be combined to give

$$\mathcal{R}_A^2 \frac{1-f_0^2}{(1-g_0)^2} \left(1 - \frac{f_0 g_0}{f_0 g_0 + f_2(1-g_0)}\right)^2 = (1-f_2^2)(1+K). \quad (12)$$

This is an implicit equation for the screen-exit velocity fraction $f_2(\mathcal{R}_A, K, f_0, g_0)$, which depends on the four parameters indicated. All the remaining $()_2$ quantities can then be computed as functions of $\mathcal{R}_A, K, f_0, g_0$ using this f_2 together with (8)–(11).

We also determine the mixed-out state V_3, p_3 , also as functions of $\mathcal{R}_A, K, f_0, g_0$, by using the mass and streamwise momentum conservation equations for the downstream flow:

$$\rho V_3 = \rho V_2 (1-g_2 + f_2 g_2) \quad (13)$$

$$p_3 + \rho V_3^2 = p_2 + \rho V_2^2 (1-g_2 + f_2^2 g_2). \quad (14)$$

Also of interest will be the displacement areas of the slower streamtube, and the blockage-fraction ratio across the vane row:

$$\Delta_0^* = A_0(1-f_0)g_0 \quad (15)$$

$$\Delta_2^* = A_2(1-f_2)g_2 \quad (16)$$

$$\mathcal{R}_{\Delta^*} \equiv (\Delta_2^*/A_2)/(\Delta_0^*/A_0) = \frac{(1-f_2)g_2}{(1-f_0)g_0} \quad (17)$$

A constant flow area with $\mathcal{R}_A = 1$ will always produce $\mathcal{R}_{\Delta^*} < 1$, which is the usual BL-thinning action of a screen. However, the present situation with $\mathcal{R}_A > 1$ can produce $\mathcal{R}_{\Delta^*} > 1$, and, hence, a thicker downstream BL if the chosen K value is relatively small. Within limits this is considered acceptable, since the primary objective of the screen here is to prevent BL separation, not to obtain a thinner BL. In a wind tunnel, the latter task is left for the flow-conditioning screens downstream of the expanding vanes.

2.3 Design considerations

A key parameter which must be selected in a given design application is the screen's K value. Larger K values improve the screen's ability to suppress flow separation and make the outlet flow

more uniform (decreased \mathcal{R}_{Δ^*}), at the cost of a greater total pressure loss (more negative C_{pT_3}). The trade-off with fixed \mathcal{R}_A and g_0 is shown in Fig. 5. The loss significantly depends on f_0 , although the K values at the knee do not change much. Hence, the chosen K would be not be strongly affected by the specific f_0 value, i.e., by the H value of the upstream BL.

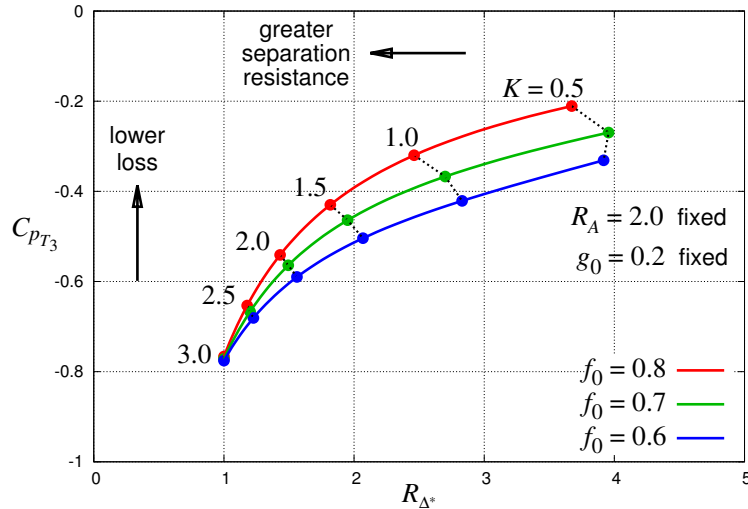


Figure 5: Trade-off between downstream total pressure and blockage-fraction ratio, versus screen K and upstream BL velocity fraction f_0

The tradeoff with fixed f_0 and g_0 , and with varying \mathcal{R}_A , is shown in Fig. 6. Here, the best choice of K at the knee of each curve is seen to strongly depend on the specific \mathcal{R}_A value. The curves also quantify the rate of increase of the losses and blockage fraction with \mathcal{R}_A , which is valuable information during design when the tunnel-size reduction benefits of increased \mathcal{R}_A need to be traded off against the increased demand on the flow screens and increased tunnel power.

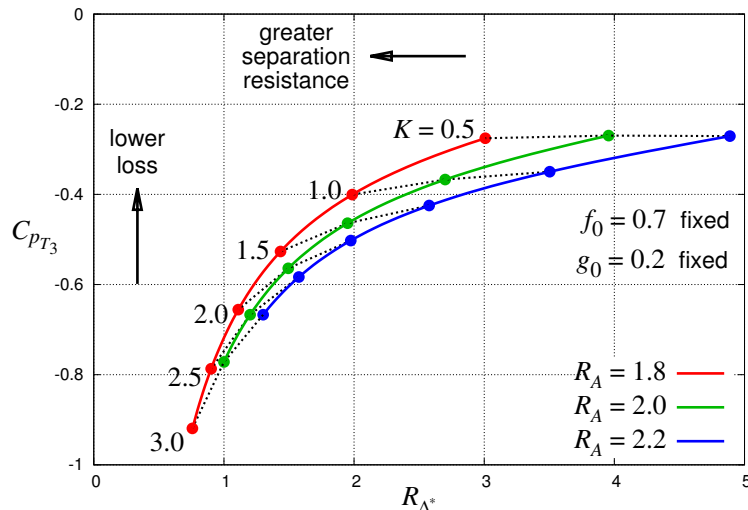


Figure 6: Trade-off between downstream total pressure and blockage-fraction ratio, versus screen K and outlet/inlet area ratio \mathcal{R}_A

Varying the remaining parameter g_0 has almost no effect, in that, the C_{pT_3} vs. \mathcal{R}_{Δ^*} curves for

any reasonable fixed \mathcal{R}_A and f_0 will nearly overlay over a range of g_0 values. Hence, this parameter does not need to be considered in design trade-offs.

3 Experimental design and setup

The success of the New WBWT critically depends on the screened expanding vane row in corner 4 working as intended, specifically without significant flow separation. To gain confidence in the design, an experimental rig simulating the entire corner 4 was constructed and tested. To obtain some “confidence margin”, the rig geometry was intentionally made more aggressive, with a rig area ratio of $\mathcal{R}_A = 2.0$ which is 6.7% larger than the 1.875 ratio of the New WBWT corner 4. Also, the turning angle was designed to be 95° , compared to 90° in any conventional wind tunnel corner.

Based on 2D MISES calculations, the vane airfoil shape was chosen to be a circular arc of 108° subtended angle, 1.0in. radius, and a constant thickness of 0.035in.. This simple geometry was chosen to enable the 42 vanes to be fabricated by cutting available thin-wall aluminum tubing. The suction side of the leading edge was shaped into a roughly 4:1 ellipse, and the trailing edges were left square. The vanes were oriented to have a -40° exit metal angle from the cascade-plane normal, with a pitch of 0.656in. The leading to trailing edge chord is $c = 1.65$ in., giving a pitch/chord ratio of 0.40. Fig. 7 shows the computed surface C_p distribution at the design inflow angle of $\arctan(2.0) = 63.43^\circ$, and a chord Reynolds number of 100 K.

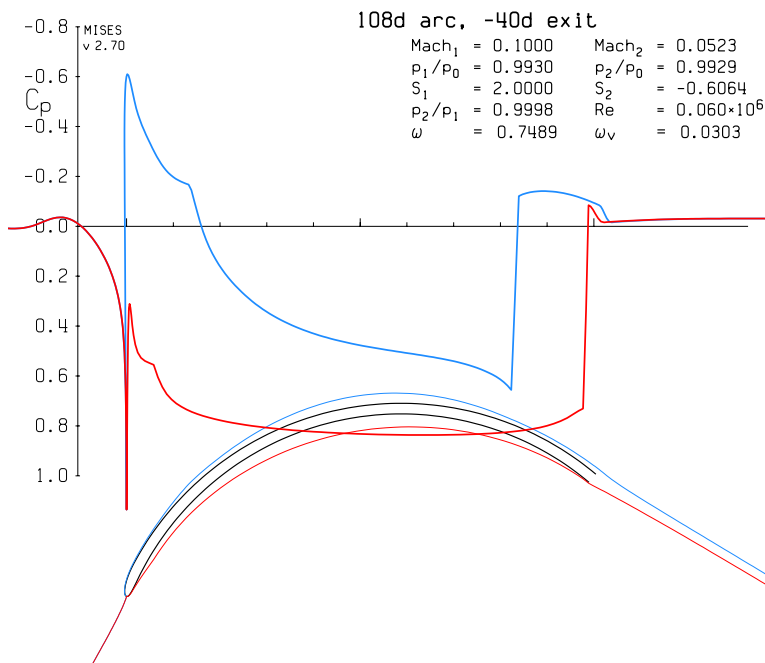


Figure 7: Computed 2D surface C_p distributions of experimental rig vanes, with specified $K = 2.3$ and $\eta = 0.58$ set to match the observed $C_{p2} = -0.05$ value at the outlet. Gap between the vane metal (black) and the adjacent colored line on each side is the displacement thickness, which thins strongly ahead of the screen

The rig is diagrammed in Fig. 8. The channel walls are 0.25in. Lexan, and the vanes are glued into slots cut into strips attached to the endwalls, flush with the interior surface. The vanes also pass through cutouts in a 0.06in. thick splitter plate at their midspan, which provides bending and torsion support for the vanes against the airloads. The screen is a 0.0037in. stainless steel wire

mesh with 74×74 /in. pitch, giving an open-area fraction of $\beta = 0.54$. The screen was bent into the required zig-zag form in a jig and glued to the vanes with RTV silicone. There are no channel walls over the outlet, so the outlet flow angle is entirely the result of loading on the vanes. The vane array can be removed from the channel, to allow flow-survey measurement of the incoming wall BLs which the vane array must handle. Figure 9 shows the rig attached to a 18×18 in. open-jet tunnel, via an adapter section which contracted the flow to the 12×18 in. cross section of the rig inlet.

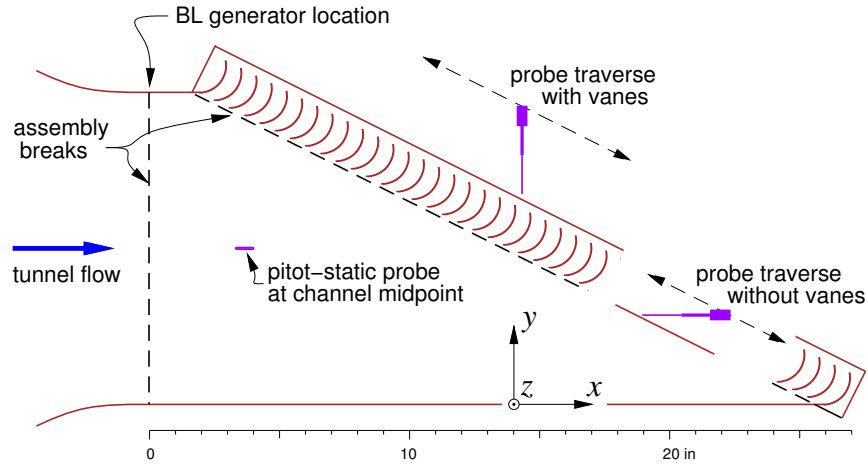


Figure 8: Top view of experimental rig. Vane-outlet screen not shown



Figure 9: Experimental rig mounted on open-jet wind tunnel, with 30-port pitot survey rake

A 5-hole probe and a 30-port total pressure rake were used in the flow surveys, using a 2D traverse system set up to cover the diagonal survey planes, as shown in Fig. 8. Pressures from the probes were measured using an ESP-32HD differential pressure scanner from A-Tech Instruments,

Ltd., with a 1psi range and $\pm 0.03\%$ resolution. All readings were referenced to room ambient pressure p_∞ , and sampled at 80Hz and averaged over 1s to provide the raw pressure data. Outputs from the upstream pitot-static probe shown in Fig. 8 were also measured together with the survey probe outputs, which gave the reference p_0 , p_{T0} , and reference dynamic pressure $\frac{1}{2}\rho V_0^2 = p_{T0} - p_0$ simultaneously with the probe data. The probe C_p and corresponding $V_2/V_0 = \sqrt{1 + C_{p_{T2}} - C_{p_2}}$ values were, therefore, very insensitive to tunnel speed drift. At 75mph inlet speed, the pressure sensor resolution is $\pm 0.3\%$ of the test inlet dynamic pressure, giving an uncertainty in the corresponding V_2/V_0 values of roughly $\pm 0.5\%$.

4 Survey measurements

4.1 Tunnel velocities

Surveys were performed at inlet flows velocities of $V_0 = 50\text{mph}$ and 75mph , to gauge the effect of Reynolds number. There were no significant differences in the measured outlet V_2/V_0 distributions between the two inlet speeds, so only the $V_0 = 75\text{mph}$ data will be presented. This inlet speed gives roughly the same experimental vane chord Reynolds number $V_0 c/\nu \simeq 10^5$ as in the actual New WBWT at a 20mph test-section speed, which is the lowest expected in typical operation. Hence, the present experiment has Reynolds numbers representative of the full scale article.

4.2 Survey display

All survey data, for cases with and without the vanes, will be plotted in the y - z -plane, which is $12\text{in.} \times 18\text{in.} = 7.27c \times 10.9c$ for the entire channel. The geometry is top/bottom symmetric about the splitter plate, and preliminary surveys indicated that the flow was also nearly symmetric. Hence, more extensive surveys were performed for the bottom half only. Preliminary surveys also indicated that the outlet velocities were lower over the outside of the corner than the inside, which is expected, since the outside inlet BL has a longer run and, hence, is thicker. Hence, surveys were focused on the lower left corner at $y, z = (0, 0)$ of the display plane, where the flow is most susceptible to separation.

4.3 Initial surveys

Initial surveys were performed with a 0.6mm diameter five-hole probe, both for the incoming BL without the vanes, and also with the vanes without and with the screen installed. The resulting velocity distributions along a few selected survey lines are shown in Fig. 10. The “peaks and valleys” in the outlet surveys correspond to the passages and vanes which have a projected pitch of $\Delta y/c = 0.178$, which was not well resolved here, resulting in the ragged distributions. Regardless, the surveys show that without the screen, the entire two vane passages near the outer wall have separated flow, and all the passages have significant separation near the bottom wall. In contrast, the presence of the screen makes the outlet flow much more uniform, and in particular, the separated flow regions are completely eliminated.

Since the five-hole probe is outside its calibration range in reverse flow, the outlet flows were also qualitatively examined with a yarn tuft on a wand. In the no-screen vane case, the tuft confirmed the presence of irregular and mostly stagnant flow over the entire outlet perimeter, with the largest stagnant regions being at the outside corners. This flow separation was of course expected, since the thick BL cannot negotiate the sudden doubling of the flow area. The static pressure rise is quantified by the outlet static pressure coefficient, which was measured with a hand-held static

probe to be approximately $C_{p2} \simeq +0.35$ (about half of the ideal inviscid value of $+0.75$). Since inlet BL fluid with $V_1/V_0 < 0.8$ has a dynamic pressure less than the observed static pressure rise, some reverse flow through the wall-adjacent passages is almost inevitable. In contrast, for the screened vanes, the tuft showed the flow direction to be the same everywhere over the outlet plane to within several degrees, with no indication of reverse flow anywhere. The measured static pressure values over the screened-vane-outlet flow are shown in Fig. 11. The averaged pressure coefficient referenced to ambient static pressure is nearly zero, which is fully consistent with the observed nearly parallel outlet flow.

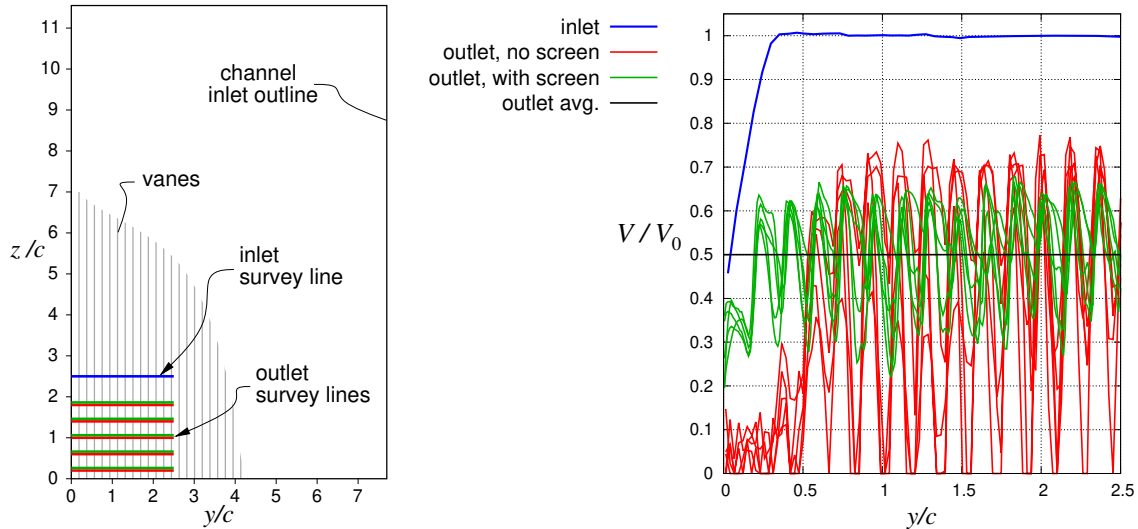


Figure 10: Inlet V_1/V_0 velocity distributions without vanes and outlet V_2/V_0 velocity distributions with no-screen and screened vanes, along the indicated survey lines. The screen eliminates all separated flow from the vane passages, even at the tunnel walls where the inlet BL is present

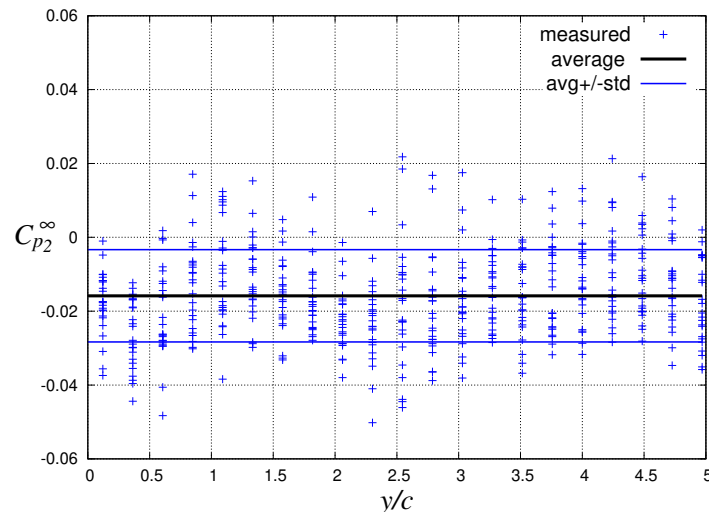


Figure 11: Measured static pressure coefficient, referenced to freestream, of the screened vanes over a portion of the outlet flow near lower left corner. The average with standard deviations is $C_{p2}^\infty \equiv (p_2 - p_\infty) / \frac{1}{2} \rho V_0^2 = -0.0158 \pm 0.0125$

4.4 Detailed surveys

Since the initial surveys revealed that with the screen installed, the outlet flow is nearly parallel, and at a nearly constant static pressure, the five-hole probe was replaced with a 30-tube pitot rake with a 0.125in. tube spacing. The velocity was then obtained from the total pressure of the rake and the ambient static pressure. Another 30-tube rake with 0.080in. spacing was also used in some cases for more spatial resolution.

All the rake tubes were sampled simultaneously using the 32-port ESP sensor (the remaining two ports sampled the upstream pitot-static). The multiple-tube sampling and the much faster settling time of the rake increased its data collection rate by two orders of magnitude over the five-hole probe, and allowed very high resolution flow surveys to be performed in a reasonable time. All the data presented below were obtained using the rakes.

5 Thin and thick inlet boundary layers

In the surveys shown in Fig. 10, the inlet wall BL thickness covers roughly two vane passages. To investigate the ability of the screened-vane cascade to negotiate much thicker BLs, spire BL generators were designed using the guidelines of Irwin[14], cut from 0.05in. aluminum sheet, and installed at the rig inflow location, as shown in Fig. 12.



Figure 12: Spire BL generators installed at rig inlet to provide relatively thick inlet wall boundary layers, which cover about 55% of the channel area. Vane array has been removed in the photo

The high-resolution measured inlet velocity distributions with and without the generators are shown in Fig. 13. The BL generators roughly quadruple the BL thickness, which now covers about nine vane passages, and all the wall BLs now cover a substantial 55% of the overall channel area. The small waviness in the velocity distribution at the outer edges of the BLs is from the individual spire wakes, which have not merged completely at the survey location. The “dent” in the unobstructed velocity distribution at $y/c = 1.2$ appears to be the remnant of a streamwise vortex originating from the corner of the tunnel adapter section. This is entirely eliminated by the BL generators.

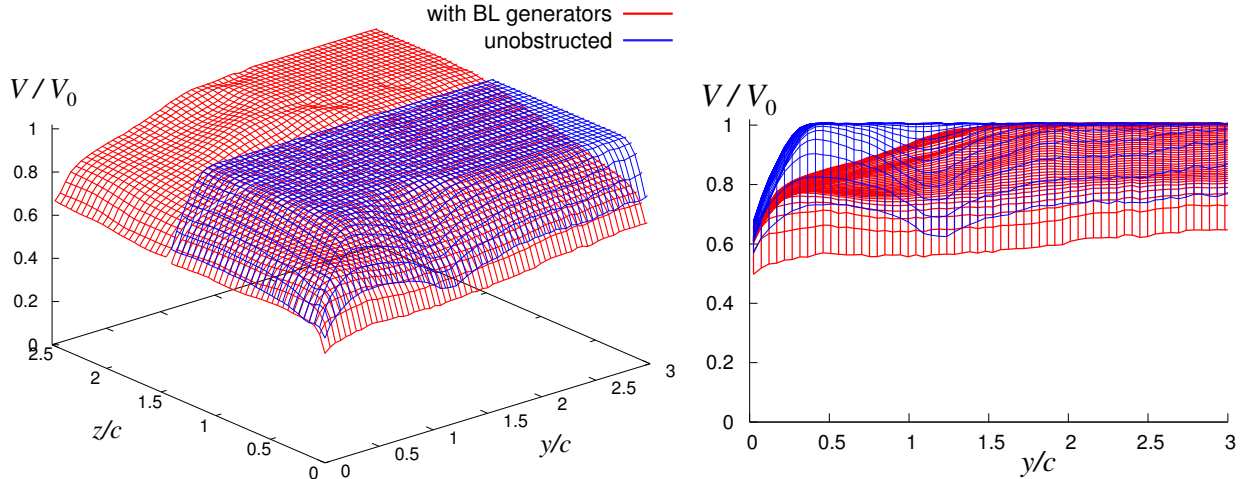


Figure 13: Measured inlet V_1/V_0 velocity distributions without vanes in the vicinity of the bottom left corner (see Fig. 14), comparing the thin inflow BLs of the unobstructed inlet with the thick layers produced by the BL generators. The uncertainty from pressure sensor resolution is estimated to be $\Delta V/V_0 = \pm 0.5\%$, which is comparable to plotting resolution here

The outlet velocity distributions for the thin and thick inlet BL flows are compared in Fig. 14. The most significant feature is that the screen acts to prevent stagnant outlet flow nearly equally well for the two cases. This corroborates the two-streamtube model results, which predict that g_0 , which is a measure of the inlet BL thickness, has little effect on the outlet flow parameters for the same $K \simeq 2.3$ value.

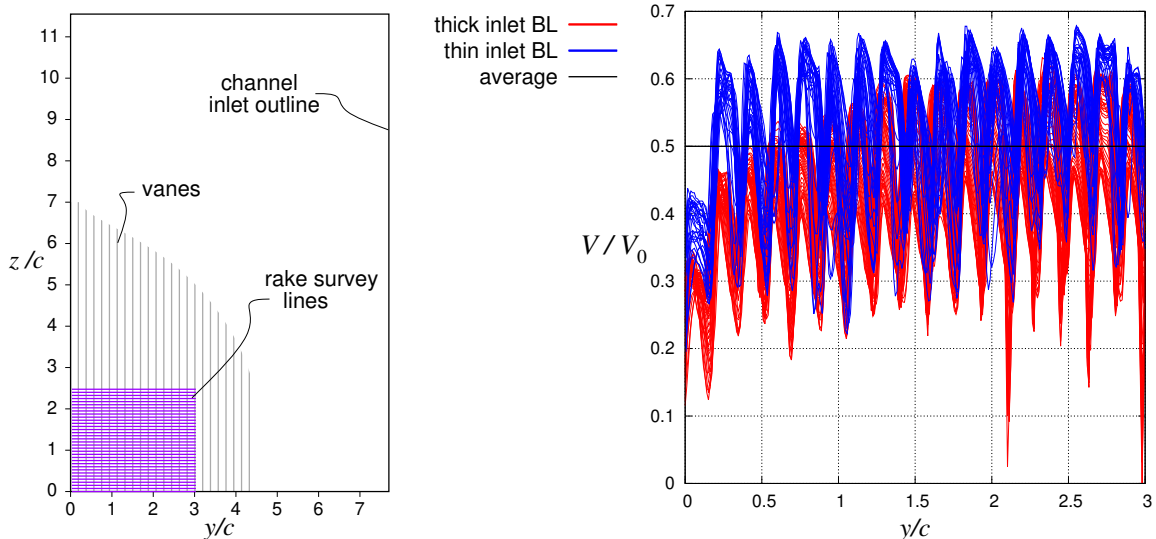


Figure 14: Measured screened-vane outlet V_2/V_0 velocity distributions for thin and thick inlet BL flows, showing the absence of separation regardless of inlet BL thickness. The “thin inlet BL” is the same flow as “outlet, with screen” in Fig. 10, but here is measured in much higher resolution with a pitot rake rather than a five-hole probe

As mentioned previously, the outlet flow direction for the screened vane cases was observed by the yarn tuft to be nearly uniform over the entire outlet plane. The angle estimated from a photo

of the tuft is roughly 96° , which is close to the $\arctan(2.0) - \arctan(-0.6104) = 94.8^\circ$ turning angle predicted by the 2D MISES calculation, as shown in Fig. 7. Some discrepancy is expected from the substantial 3D effects near the walls.

6 3D CFD simulations

6.1 Case setup

To investigate the effects of the design parameters, in particular the screen K value, the flow in the experimental rig was simulated in ANSYS [11] using the RANS equations. For computational economy, only the bottom outer quadrant was simulated, using 20 vane passages of half span, with inviscid walls representing the symmetry planes. The effect of the screen was implemented by the body force model defined by equations (3)–(5). The $K = 2.2$ value in the initial calculation was set, such that the computed outlet C_p closely matched the $C_{p_2} = -0.05$ value which corresponds to the measured outlet $C_{p_2}^\infty = -0.0158$ shown in Fig. 11. The relation between the two pressure coefficients is:

$$C_{p_2} = C_{p_2}^\infty - (p_0 - p_\infty) / \frac{1}{2} \rho V_0^2, \quad (18)$$

and the required last term was obtained directly from the $p_0 - p_\infty$ and $p_{T_0} - p_\infty$ gauge pressures taken from the upstream pitot-static probe.

The $\eta = 0.58$ value was specified based on the correlation of Livesey and Laws [15], although this parameter will have little effect in this case, since the flow is almost normal to the screen. In the calculation, the BLs start at the channel inlet, so the inlet length was adjusted, so that the resulting BL profiles at the vane inlet location (with the vanes absent) matched the experimentally measured profiles as closely as possible.

6.2 Calculated outlet flows

The computed and measured outlet velocity contours are compared in Fig. 15. Profiles along several z locations (see Fig. 8) are also shown in Fig. 16. The rather good match gives some confidence that the 3D CFD calculations can be relied upon to perform the parameter studies presented next.

6.3 Effects of screen pressure drop coefficient

The design trade-offs in the selection of the screen pressure drop coefficient K , as predicted by the simple 2D inviscid model, were shown in Figs. 5 and 6. To verify these design trend predictions for viscous 3D flows, a sequence of 3D CFD cases was run with the K value progressively decreased, until significant outlet separated flow was obtained. The computed outlet velocity contours are shown in Fig. 17, and the corresponding profiles are shown in Fig. 18.

These 3D CFD results corroborate and “calibrate” the trends predicted by the two-streamtube 2D model. Specifically, the CFD results indicate that for this $\mathcal{R}_A = 2.0$ case, significant separation will start to appear for $K < 1.5$ roughly, which, in Figs. 5 and 6, is seen to correspond to $\mathcal{R}_{\Delta^*} > 2.0$. For the New WBWT which has $\mathcal{R}_A = 1.875$, Fig. 6, in turn, then suggests that a screen with $K \geq 1.25$ will be needed to obtain the same $\mathcal{R}_{\Delta^*} \simeq 2.0$ ratio, and the same separation-onset threshold.

Fig. 19 shows the mixed-out total pressure coefficient $C_{p_{T_3}}$ for a range of K values, and for two inlet BL thickness ratios. Since the 1D model does not account for the losses of the vane BLs, its $C_{p_{T_3}}$ curves have been offset by -0.08 , which is the additional vane total pressure loss estimated by 2D MISES calculations. Also shown are the $C_{p_{T_3}}$ extracted from the 3D CFD solutions, using the

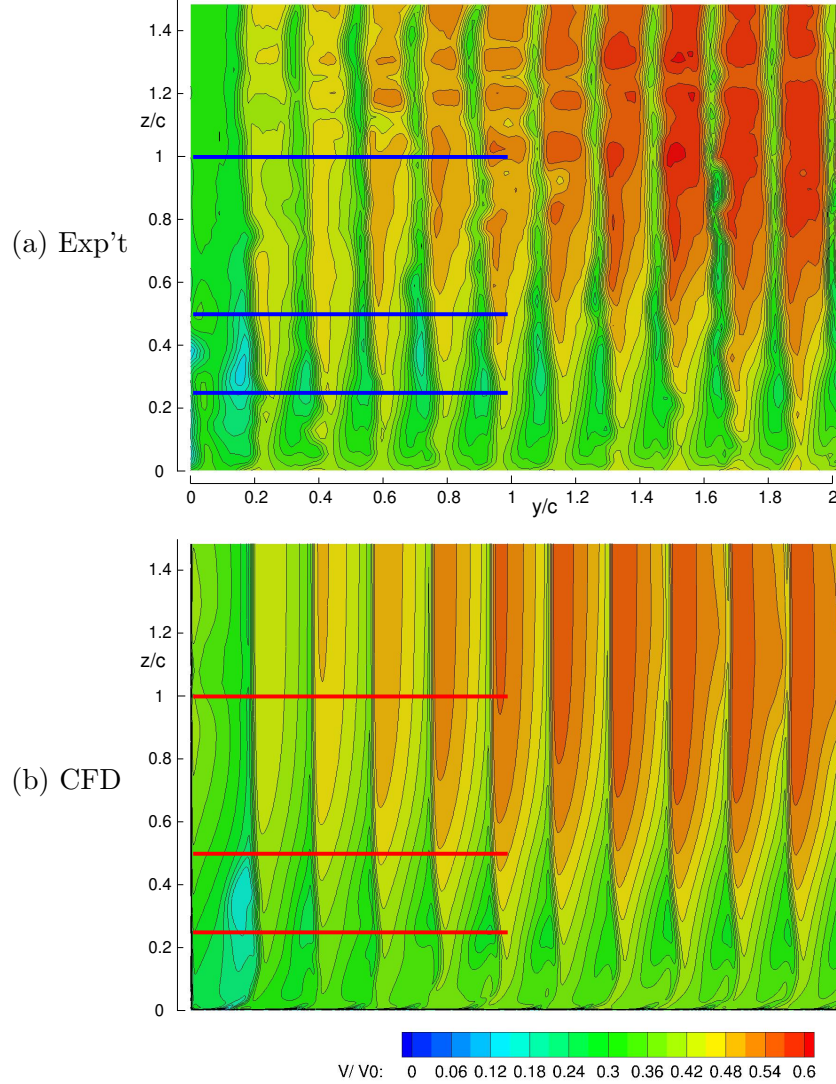


Figure 15: Comparison of experimental and CFD outlet velocity ratio V_2/V_0 in the vicinity of the bottom left channel corner. The inflow BLs are along the left and bottom plot edges. Red and blue horizontal lines indicate slices for line plots in Fig. 16

mass and momentum conservation Eqs. (13) and (14), integrated over the CFD outlet flow plane. The model captures the basic trend of loss versus K reasonably well.

7 Conclusions

This paper presented a new screened expanding vane concept which enables simultaneous turning and diffusion in an effectively negligible streamwise distance. A simple parallel-streamtube model of the flow was developed to investigate the effects of the key design parameters, and computational simulations and experimental measurements confirm that the concept works as intended. When implemented as the fourth corner of a closed-circuit wind tunnel, it enables a dramatic reduction of the overall tunnel space footprint compared to traditional wind tunnel designs of the same capability.

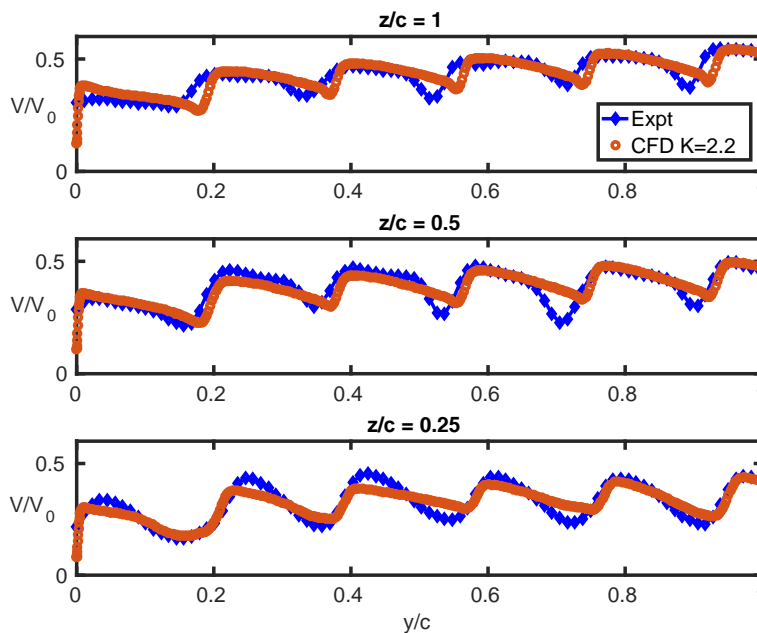


Figure 16: Line plots of outlet V_2/V_0 velocities in Fig. 15, at three z/c location slices

Acknowledgements

The authors are grateful to Linda Hedges, Aaron Bucher, and Scott Eberhardt of Amazon Web Services (AWS) for providing both computational resources and much assistance on the AWS computing platform. We are also grateful to Chris Hill, Dipankar Choudhury, and Ryan Gordon of ANSYS for the provision of Fluent software for this study. Finally, we are grateful to David Robertson and Annika Rollock of MIT for the assistance with the experimental setup.

References

- [1] P. Bradshaw and R. C. Pankhurst. The design of low-speed wind tunnels. *Prog Aerosp Sci*, 5:1–69, 1964.
- [2] H.B. Squire and H. Hogg. Diffuser-resistance combinations in relation to wind tunnel design. Technical Report RAE Report No. Aero 1933, RAE, 1944.
- [3] G.B. Schubauer and W.G. Spangenberg. Effect of screens in wide-angle diffusers. Technical Report Report 949, NACA, June 1947.
- [4] R. D. Mehta. The aerodynamic design of blower tunnels with wide-angle diffusers. *Progress in Aerospace Sciences*, 18:59–120, 1977.
- [5] B. Lindgren and A. V. Johannson. Evaluation of a new wind tunnel with expanding corners. *Exp Fluids*, 36:197–203, 2004.
- [6] B. Lindgren, J. Osterlund, and A. V. Johannson. Measurement and calculation of guide vane performance in expanding bends for wind-tunnels. *Exp Fluids*, 24:265–272, 1998.
- [7] V.M. Lei, Z.S. Spakovszky, and E.M. Greitzer. A criterion for axial compressor hub-corner stall. *J Turbomach*, 130(3):031006–1 – 031006–10, July 2008.
- [8] E.M. Greitzer, C.S. Tan, and Graf M.B. *Internal flow — concepts and applications*. Cambridge University Press, Cambridge, UK., 2004.

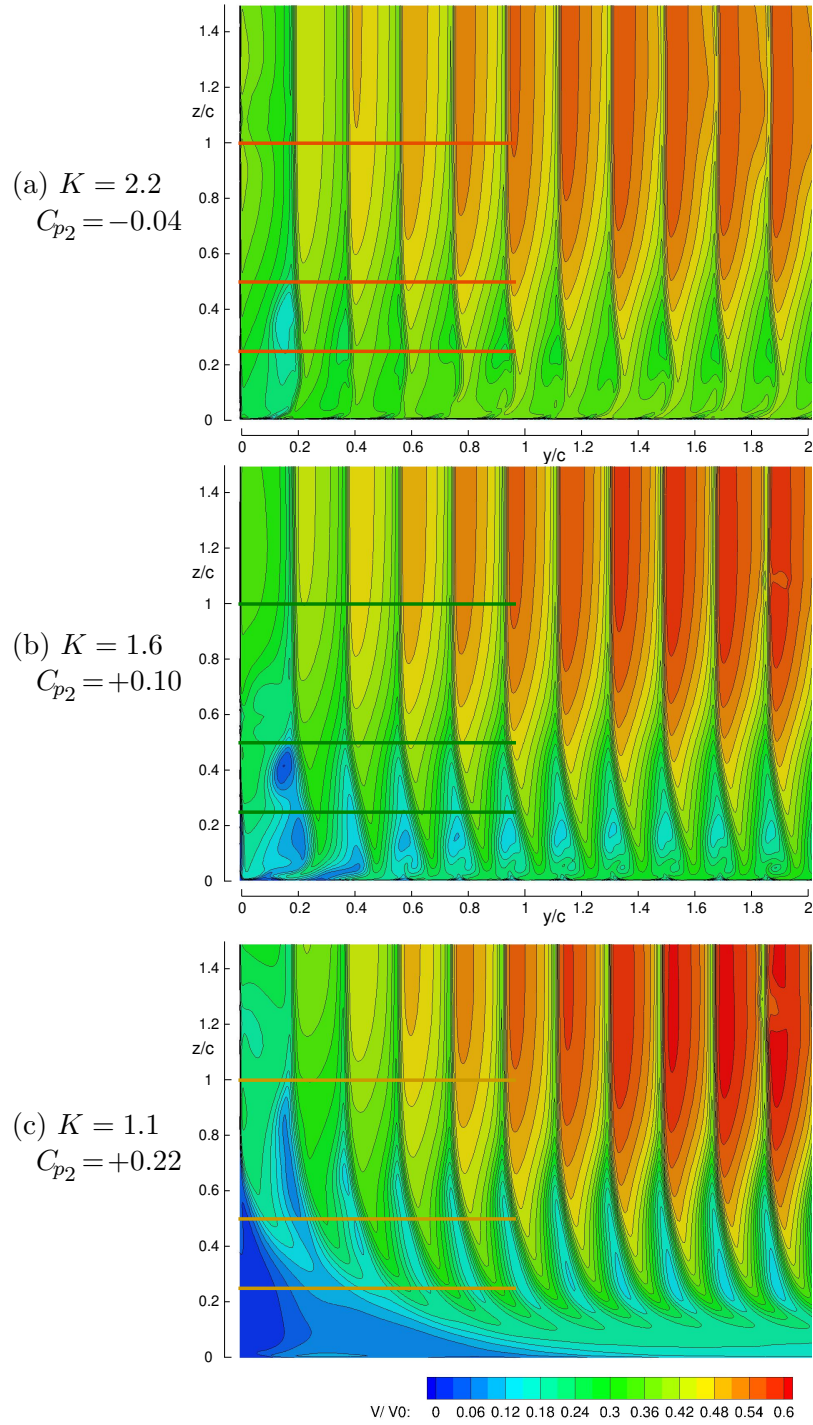


Figure 17: Computed outlet V_2/V_0 velocity contours for thick inlet BL, for three K values, and corresponding computed outlet static C_{p_2} values. Significant corner separation appears for the lowest K value. Colored horizontal lines indicate slices for line plots in Fig. 18

[9] J.W. Elder. Steady flow through non-uniform gauzes of arbitrary shape. *J Fluid Mech*, 5:355–368, 1959.

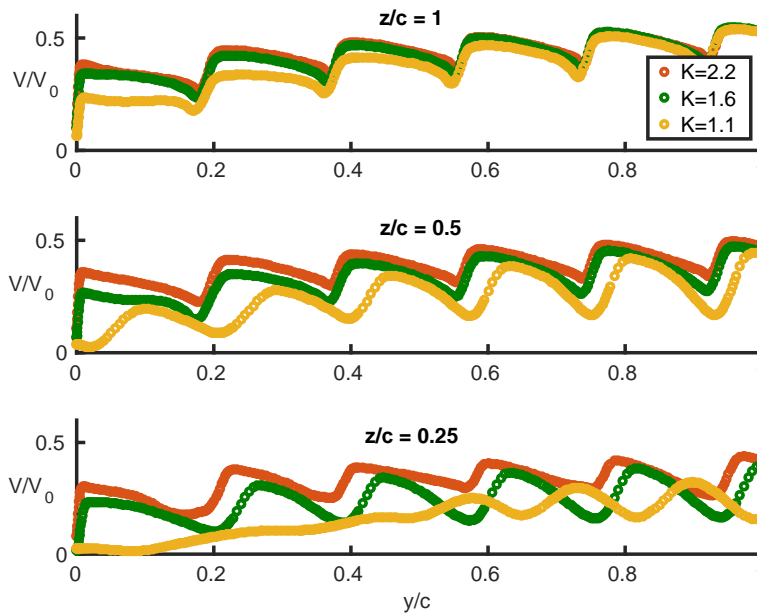


Figure 18: Line plots of computed outlet V_2/V_0 velocities in Fig. 17, at three z/c location slices

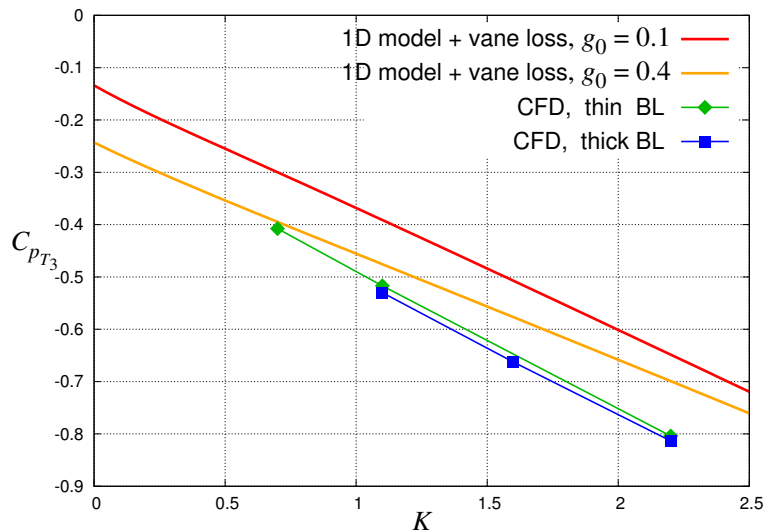


Figure 19: Loss versus screen pressure drop coefficient, as predicted by 1D model (with added estimated 2D vane loss), and as extracted from CFD solutions

- [10] C.L. Gentry, P.F. Quinto, G.M. Gatlin, and Z.T. Applin. The Langley 14- by 22-foot subsonic tunnel: description, flow characteristics, and guide for users. Technical Report NASA-TP-3008, NASA, Sept 1990.
- [11] ANSYS. Ansys-fluent. <https://www.ansys.com/products/fluids/ansys-fluent>, April 2018.
- [12] M.B. Giles and M. Drela. Two-dimensional transonic aerodynamic design method. *AIAA J*, 25(9):1199–1206, Sep 1987.
- [13] M. Drela. Aerodynamics of heat exchangers for high-altitude aircraft. *J Aircr*, 33(2):176–184, Mar-Apr 1996.

- [14] H.P.A.H. Irwin. The design of spires for wind simulation. *J Wind Eng Ind Aerodyn*, 7(3):361–366, 1981.
- [15] J.L. Livesey and E.M. Laws. Flow through non-uniform gauze screens. *J Fluid Mech*, 59:737–743, 1973.